Supporting Information

McGraw et al. 10.1073/pnas.1513565113

Experimental Error and Model Deviations

We note that relative deviations between profiles predicted by the NYM and those measured with AFM are up to 5% (Fig. 2, main text). Because the typical contact angles are rather high, $\theta \approx 60°$, overshoot can affect the absolute height measurement in the forward and reverse directions. We show an example of this overshoot in Fig. S4, where the feedback parameters that control the interaction between the AFM tip and the substrate and droplet surfaces are tuned to minimize the difference between forward and reverse traces, while allowing for a minimum tip penetration (63). The typical deviations associated with various instrumental effects for the parameter settings of this scan (and those presented in the rest of the paper) are thus on the order of 1%. However, independent checks on static profiles have shown that the overshoot presented here is rate dependent, and can lead to variations on the height of 5%. Thus, the overall error on the height measurement at the ridge is roughly the same as the discrepancy between experiment and the NYM. Based on the profiles alone, a discrepancy between the NYM and the experiments cannot be resolved.

Although we cannot rule out other models that would change predicted profile shapes beyond the resolution of the current measurements (i.e., $\sim 5\%$ relative error), our numerical model with Navier slip and Young-angle boundary condition has quantitatively corroborated the experimental height profile evolutions. Furthermore, the NYM and the scaling approaches have captured the main features of the contact line dynamics. However, we caution that the agreement is not quantitative in all respects. At small b/R_∞, the experimental time constants in Fig. 4D deviate from the NYM data and the scaling asymptotics. Several effects may explain this discrepancy: nonlinear (28) or spatially nonuniform (29, 30) slip may be operative; the assumption of constant microscopic contact angle (17, 18), $\theta(t) = \theta_\infty$, could be relaxed as well (Fig. S3); furthermore, in ultrathin (~ 5 nm) dewetting polymer films, thermal fluctuations are known to enhance the dynamics (64), which could also affect the effective liquid mobility at the solid–liquid boundary, or at the three-phase contact line. Additionally, at relatively small slip length, other mechanisms of CLM may contribute (16). The present results thus open a perspective to more detailed studies from both theoretical and experimental sides.

Asymptotic Early-Time Scaling

Here, we provide quantitative arguments for the scaling law given in Eq. 2, using lubrication theory. Because the experiments are performed in a situation where the slip length b is comparable to the initial droplet radius R_0, and because we focus on the short-term asymptotic behavior near the contact line, we invoke the 2D thin-film equation for intermediate slip (65):

$$\partial_t h + \frac{\gamma b}{\eta} \, \partial_x \left(h^2 \partial_x^3 h \right) = 0, \qquad \text{[S1]}$$

where γ is the PS–air surface tension and η the PS shear viscosity. This partial differential equation describes the viscocapillary evolution of a thin liquid film of profile $h(x,t)$ in space x (coordinate taken in the frame of the substrate) and time t, with intermediate slip at the substrate. The contact line is located at $x = R(t)$, and the liquid film is chosen to occupy the $x < R(t)$ region. The two boundary conditions at the contact line are thus $h(R(t),t) = 0$ and $\partial_x h(R(t),t) = -\tan\theta_\infty$. We thus assume an equilibrium microscopic contact angle θ_∞ at any time, consistent with the NYM used in the numerics. Let

us nondimensionalize the problem through $x = XR_0$, $t = T\eta R_0^2/\gamma b$, $R(t) = \mathcal{R}(T)R_0$, $h(x,t) = H(X,T)R_0$, such that

$$\partial_T H + \partial_X \left(H^2 \partial_X^3 H \right) = 0. \qquad \text{[S2]}$$

We now look for a self-similar asymptotic form at short times near the contact line:

$$H(X,T) = T^\alpha F\left(\widetilde{U}\right), \qquad \text{[S3]}$$

$$\widetilde{U} = \frac{X - \mathcal{R}(T)}{T^\beta}, \qquad \text{[S4]}$$

where α and β are unknown exponents, and $\mathcal{R}(T)$ is the law of interest. Invoking the boundary conditions above, one obtains $\alpha = \beta$, $F(0) = 0$, and $F'(0) = -\tan\theta_\infty$. Then, injecting the self-similar form into Eq. S2, one gets

$$\alpha\left(F - \widetilde{U}F'\right) = \dot{\mathcal{R}}T^{1-\alpha}F' - T^{1-2\alpha}\left(F^2 F'''\right)', \qquad \text{[S5]}$$

where the prime represents the derivative with respect to $\widetilde{U}$, and the dot represents the derivative with respect to T. The proposed self-similar form is a possible solution if and only if the previous equation is an ordinary differential equation (ODE) on the single variable $\widetilde{U}$. One possibility is thus given by $\alpha = 1/2$, together with

$$\mathcal{R} = 1 - C\sqrt{T}, \qquad \text{[S6]}$$

which satisfies the initial condition, where C is a positive numerical constant, and where the minus sign corresponds to the dewetting situation. In that case, the ODE satisfied by F reads

$$F + \left(C - \widetilde{U}\right)F' + 2\left(F^2 F'''\right)' = 0. \qquad \text{[S7]}$$

The latter could be solved numerically by adding three boundary conditions—especially in the unperturbed far-field region—and by shooting on C. Finally, putting back real dimensions, one obtains

$$R_0 - R(t) = C\sqrt{\frac{\gamma b t}{\eta}}, \qquad \text{[S8]}$$

which demonstrates the scaling law of Eq. 2 in the main text. Furthermore, one can validate the proposed self-similar form by comparison with the experimental profiles, as shown in Fig. S6.

We note that the essential ingredients in both the power balance and the thin-film equation are the same: capillarity drives a viscous flow and the dissipation is mostly due to friction at the substrate. The fact that we neglected the H^3 term in the thin-film equation, according to the intermediate-slip model (65), is consistent with the fact that we also neglected the bulk viscous dissipation near the contact line in the power balance leading to the scaling of Eq. 2.

Asymptotic Late-Time Scalings

We will assume that the shape of the contracting droplet is close to that of a spherical cap. In the late-time regime of the contraction process, the apparent contact angle θ (evaluated through the assumed spherical cap profile) deviates from the microscopic contact angle θ_∞, but the difference $\theta - \theta_\infty$ is small and approaches nil at asymptotically large times.

The interfacial energy of a spherical cap with an apparent contact angle θ is given by

$$E = \gamma(A_{lv} - \cos\theta_\infty A_{sl}), \qquad \text{[S9]}$$

where we have defined the area of the substrate wet by liquid,

$$A_{sl} = \pi R^2, \qquad \text{[S10]}$$

and the interfacial area between the liquid spherical cap and the vapor phase,

$$A_{lv} = \frac{2\pi(1 - \cos\theta)R^2}{\sin^2\theta}. \qquad \text{[S11]}$$

The contact line radius R is linked to the apparent contact angle θ by the condition that the volume of the liquid,

$$\Omega = \frac{\pi(1 - \cos\theta)^2(2 + \cos\theta)R^3}{3\sin^3\theta}, \qquad \text{[S12]}$$

is constant.

We first invert Eq. **S12** to obtain

$$R = \left[\frac{3\Omega\sin^3\theta}{\pi(1-\cos\theta)^2(2+\sin\theta)}\right]^{1/3}, \qquad \text{[S13]}$$

and insert the latter into Eqs. **S10** and **S11**. We thus obtain from Eq. **S9** the total interfacial energy of the spherical cap $E(\theta)$ as a function of the apparent contact angle θ only. We find

$$\left.\frac{dE}{d\theta}\right|_{\theta=\theta_\infty} = 0, \qquad \text{[S14]}$$

as expected in mechanical equilibrium for $\theta = \theta_\infty$, and a second derivative

$$\left.\frac{d^2E}{d\theta^2}\right|_{\theta=\theta_\infty} = \frac{2\pi R_\infty^2}{2 + \cos\theta_\infty} > 0, \qquad \text{[S15]}$$

because the spherical cap is a stable shape.

Similarly, we could use an energy $\widetilde{E}(R)$ that depends only on the radius of the contact line R and $\theta(R)$. The results are

$$\left.\frac{d\widetilde{E}}{dR}\right|_{R=R_\infty} = 0, \qquad \text{[S16]}$$

and

$$\left.\frac{d^2\widetilde{E}}{dR^2}\right|_{R=R_\infty} = 2\pi(2 + \cos\theta_\infty)\sin^2\theta_\infty > 0. \qquad \text{[S17]}$$

Here, we make use of the chain rule of differentiation:

$$\left.\frac{d\widetilde{E}}{dR}\right|_{R=R_\infty} \equiv \left.\frac{dE}{d\theta}\right|_{\theta=\theta_\infty} \left(\frac{dR}{d\theta}\right)^{-1}\Bigg|_{\theta=\theta_\infty}, \qquad \text{[S18]}$$

and the identity

$$\left.\frac{d^2\widetilde{E}}{dR^2}\right|_{R=R_\infty} \equiv \left.\frac{d^2E}{d\theta^2}\right|_{\theta=\theta_\infty} \left(\frac{dR}{d\theta}\right)^{-2}\Bigg|_{\theta=\theta_\infty}, \qquad \text{[S19]}$$

which holds for an equilibrium state at $\theta = \theta_\infty$ and $R = R_\infty$.

Expanding the energy $\widetilde{E}(R)$ around $R = R_\infty$ up to second order yields

$$\widetilde{E} = \widetilde{E}_\infty + \pi\gamma(2 + \cos\theta_\infty)\sin^2\theta_\infty (R - R_\infty)^2, \qquad \text{[S20]}$$

which, when differentiated with respect to $R - R_\infty$, yields a linear restoring force as claimed in the main text. The injected power from the gain of interfacial energy then reads

$$\mathcal{P}_{inj} = 2\pi\gamma(2 + \cos\theta_\infty)\sin^2\theta_\infty (R - R_\infty)\dot{R}. \qquad \text{[S21]}$$

Weak Slip: $b \ll R$. In the limit of weak slip, the dissipation is mainly due to viscous losses in the bulk flow close to the contact line. In this contact line region, the free-surface profile of the droplet is assumed to be a wedge described by $z = h(x, t) = x\theta$, where x denotes the distance from the contact line. When the droplet spreads with a contact line velocity $\dot{R}$, there is a flow in the wedge that is described by a Poiseuille velocity profile:

$$v = \frac{3\dot{R}}{2h^2} z(z - 2h), \qquad \text{[S22]}$$

with a local average velocity $(\int_0^h dz\, v)/h = \dot{R}$, and where we assumed a no-slip boundary condition at the substrate and a no-shear boundary condition at the free surface. The partial-slip boundary condition gives a noticeable departure from the Poiseuille profile only in the vicinity of the contact line where $h(x) \lesssim \theta\ell_m$, with a microscopic length, $\ell_m = \widetilde{C} b$, where $\widetilde{C} \sim \mathcal{O}(1)$. Therefore, the viscous dissipation power reads

$$\mathcal{P}_{dis} = 2\pi\eta R_\infty \int_{\ell_m}^{R_\infty} dx \int_0^h dz\, (\partial_z v)^2 = \frac{6\pi\eta R_\infty\dot{R}^2}{\theta_\infty}\ln\left(\frac{R_\infty}{\widetilde{C} b}\right). \qquad \text{[S23]}$$

Balancing the dissipated power, Eq. **S23**, and the injected power, Eq. **S21**, yields a differential equation for $R(t)$ with the solution

$$R(t) - R_\infty \sim \exp\left(-\frac{t}{\tau}\right), \qquad \text{[S24]}$$

with a time constant

$$\tau = \frac{\gamma R_\infty}{\eta} f(b/R_\infty), \qquad \text{[S25]}$$

$$f(b/R_\infty) = -\frac{3\ln(b/R_\infty)}{\theta_\infty(2 + \cos\theta_\infty)\sin^2\theta_\infty} + C_1, \qquad \text{[S26]}$$

where C_1 is a nonuniversal constant that depends on the global interfacial geometry. Identifying Eq. **S26** with the corresponding expression in the main text, $f = C_0\ln(b/R_\infty) + C_1$, and substituting $\theta_\infty = 62°$, we find $C_0 = 1.44$.

Strong Slip: $b \gg R$. Because of incompressibility we have $\text{Tr}(\dot{\epsilon}) = 0$ for the rate-of-strain tensor $\dot{\epsilon}$. For flat droplets $\theta_\infty \ll 1$, we can assume an axially symmetric and uniform straining flow in the horizontal and vertical direction of the droplet. In particular, we find that the rate of strain $\dot{\epsilon}_z$ into the axial direction is twice the rate of strain in the two directions parallel to the substrate:

$$\dot{\epsilon}_x = \dot{\epsilon}_y = -\frac{\dot{\epsilon}_z}{2}. \qquad \text{[S27]}$$

For a Newtonian fluid, we have $\boldsymbol{\sigma} = \eta\dot{\epsilon}$, which provides us with the viscous dissipation:

$$\mathcal{P}_{\text{dis}} = \int dV \, \boldsymbol{\sigma} : \dot{\boldsymbol{\epsilon}}, \qquad \text{[S28]}$$

which yields

$$\mathcal{P}_{\text{dis}} = 12 \, \eta \, \dot{\epsilon}^2 \, \Omega, \qquad \text{[S29]}$$

where the volume Ω is given by Eq. S12. Balancing the injected power of Eq. S21 with the dissipated power of Eq. S29,

and relations $\dot{R}/R = \dot{\epsilon}_x = \dot{\epsilon}_y$, we finally arrive at the relaxation timescale:

$$\tau(\theta_\infty) = \frac{\eta R_\infty}{\gamma} \frac{2(1 - \cos\theta_\infty)^2}{\sin^5\theta_\infty}, \qquad \text{[S30]}$$

valid in the limit of full slip $b/R_\infty \to \infty$. For the particular case considered here, we have

$$\tau(62°) \approx 1.05 \, \frac{\eta R_\infty}{\gamma}. \qquad \text{[S31]}$$
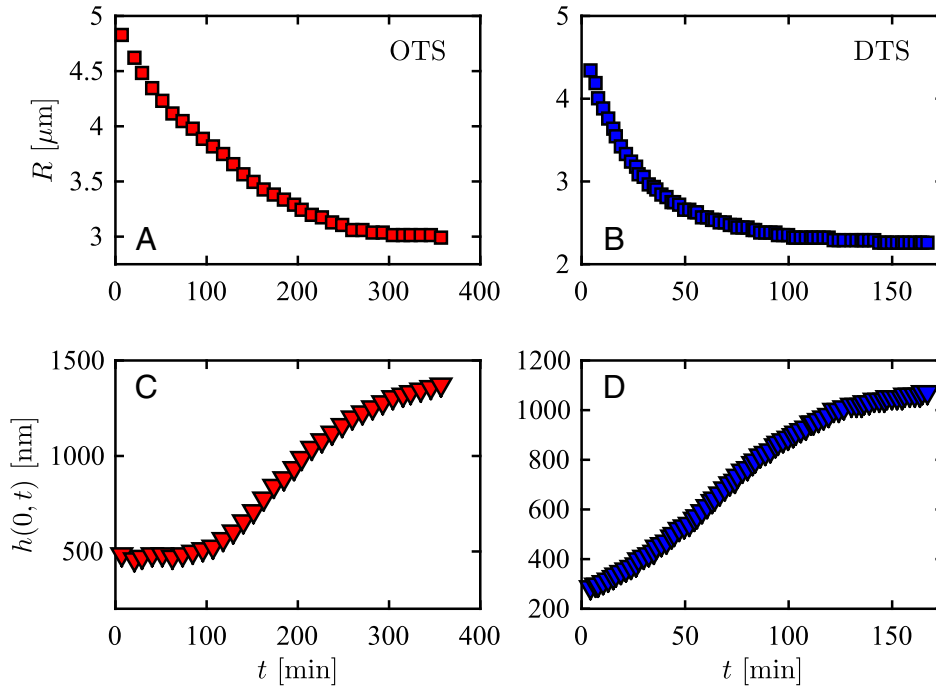

Fig. S1. Experimental contact line radius for the 10.3-kg/mol PS droplets dewetting from OTS (*A*) and DTS (*B*), as shown in Fig. 1 of the main text. (*C* and *D*) Central height evolutions for the same droplets. Note the approximately constant central height for the droplet on (*C*) OTS (smaller slip, see main text) at early times, compared with the central height for the droplet on (*D*) DTS (larger slip, see main text) whose height is increasing from the first experimentally accessible time.
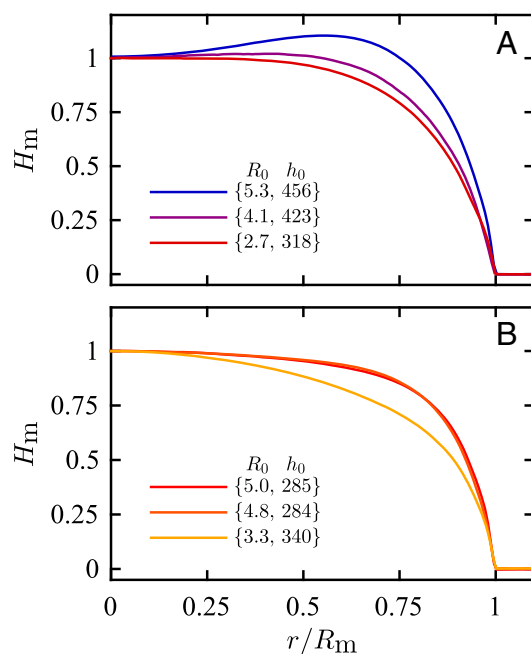
Fig. S2. (*A*) Experimental AFM data for PS microdroplets dewetting from OTS; here, $H_m(r/R_m) = h(r, t_m)/h(0, t_m)$, where the subscript "m" refers to the time when the height profile achieves maximal deviation from a spherical cap (compare gray lines in Fig. 1 of the main text). The legend shows the initial contact line radius, R_0 in micrometers and the initial central height, h_0, in nanometers. The ridge disappears for an initial contact line radius in the range 2.7 μm < R_0 < 4.1 μm (slip length, $b_{OTS} \approx 160$ nm). (*B*) Conversely, the ridge does not appear for droplets with $R_0 \approx 5$ μm and below when dewetting from DTS ($b_{DTS} \approx 2,250$ nm), even while the initial contact angle, θ_0, is slightly smaller in the DTS case.
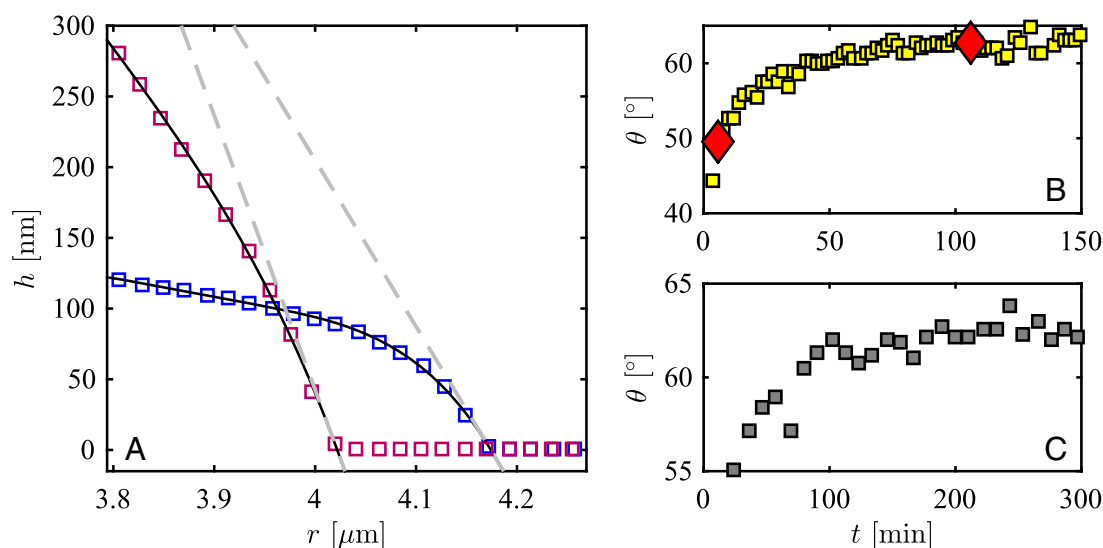

Fig. S3. (*A*) Experimental height profiles of a dewetting PS droplet on DTS (compare Fig. 1 of the main text), from which contact angles, $\theta(t)$, can be obtained. The tangents (dashed gray lines) of a fourth-order polynomial fit to the data (solid lines, not all fitted data shown) at the substrate, i.e., at $h = 0$, are obtained. The curve with larger contact angle has been shifted horizontally for clarity. (*B*) Contact angle as a function of time for the droplet represented in *A*. Red lozenges indicate the curves shown in *A*. We note that the initial angle (before dewetting starts) is $\theta_0 \approx 7°$. (*C*) Contact angle as a function of time for the PS droplet on OTS shown in Fig. 1 of the main text.
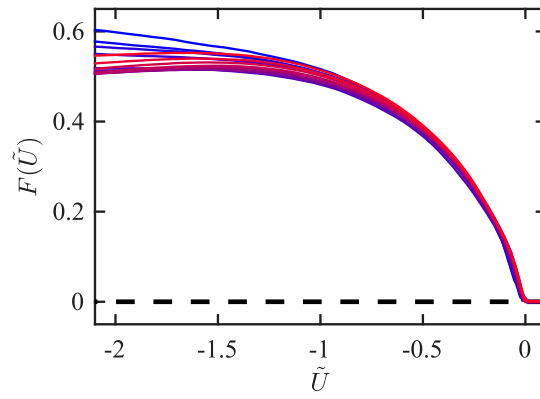
Fig. S4. Full height profiles for the forward (blue, left to right) and backward (red, right to left) traces of the AFM tip over a 10-kg/mol PS droplet dewetting from OTS at 110 °C. Contact angles as shown in Fig. S3 are only measured in directions where there is no overshoot on the substrate.

Fig. S5. (*Top*) Squared slip velocity (i.e., the fluid velocity at the substrate) as a function of the radial position, normalized by the contact line radius. The dimensionless slip lengths are the same as those for the droplets shown in Fig. 2 of the main text. (*Bottom*) Normalized frictional dissipation power (i.e., the dissipation due to fluid sliding against the solid substrate) on a disk of size r as a function of the normalized radial coordinate. The dashed line represents $y = 1 - x$ with y the vertical coordinate and x the horizontal one. The points at which the solid lines cross the dashed one are always below $y = 0.5$, which demonstrates that most of the frictional dissipation occurs near the contact line for both cases, especially at early times (blue).

Fig. S6. Self-similar representation (Eqs. **S3** and **S4**) of early-time profiles for a 10-kg/mol PS droplet at 110 °C dewetting on a Si substrate coated with OTS, for times 20 min $< t <$ 160 min.